Torsional fracture of viscoelastic liquid bridges

San To Chan[a,1], Frank P. A. van Berlo[b,1], Hammad A. Faizi[c,1], Atsushi Matsumoto[a], Simon J. Haward[a], Patrick D. Anderson[b,d], and Amy Q. Shen[a,2]

[a]Micro/Bio/Nanofluidics Unit, Okinawa Institute of Science and Technology Graduate University, Okinawa 904-0495, Japan; [b]Department of Mechanical Engineering, Eindhoven University of Technology, MB Eindhoven 5600, The Netherlands; [c]Department of Mechanical Engineering, Northwestern University, Evanston, IL 60208; and [d]Institute for Complex Molecular Systems, Eindhoven University of Technology, 5600MB Eindhoven, The Netherlands

Edited by David A. Weitz, Harvard University, Cambridge, MA, and approved May 10, 2021 (received for review March 11, 2021)

Short liquid bridges are stable under the action of surface tension. In applications like electronic packaging, food engineering, and additive manufacturing, this poses challenges to the clean and fast dispensing of viscoelastic fluids. Here, we investigate how viscoelastic liquid bridges can be destabilized by torsion. By combining high-speed imaging and numerical simulation, we show that concave surfaces of liquid bridges can localize shear, in turn localizing normal stresses and making the surface more concave. Such positive feedback creates an indent, which propagates toward the center and leads to breakup of the liquid bridge. The indent formation mechanism closely resembles edge fracture, an often undesired viscoelastic flow instability characterized by the sudden indentation of the fluid's free surface when the fluid is subjected to shear. By applying torsion, even short, capillary stable liquid bridges can be broken in the order of 1 s. This may lead to the development of dispensing protocols that reduce substrate contamination by the satellite droplets and long capillary tails formed by capillary retraction, which is the current mainstream industrial method for destabilizing viscoelastic liquid bridges.

edge fracture | viscoelasticity | liquid bridge | flow instability | contact printing

Industries such as electronic packaging, food engineering, and additive manufacturing require high-speed and precision dispensing of functional fluids, which are usually viscoelastic (1–6), i.e., with properties between viscous fluids and elastic solids. During the dispensing process, a liquid bridge connecting the nozzle and substrate is formed (schematics in Fig. 1*A*). With nozzle radius R_n, liquid bridge volume V, height H, density ρ, surface tension σ, and gravitational acceleration g, the liquid bridge stability depends on the dimensionless volume $\mathcal{V} = V/\pi R_n^2 H$, aspect ratio $\Lambda = H/2R_n$, and Bond number $\mathrm{Bo_n} = \rho g R_n^2/\sigma$ (ratio of gravitational to capillary stresses). The stability region of $\{\mathcal{V}, \Lambda\}$ shrinks as $\mathrm{Bo_n}$ increases. As an example, for a liquid bridge with $0.5 < \mathcal{V} < 1$ and $\mathrm{Bo_n} = 5$, the nozzle must be retracted above a critical height $H_c \approx R_n$ such that the liquid bridge becomes unstable (7).

Once the viscoelastic liquid bridge becomes unstable, its thinning dynamics can be characterized by four dimensionless parameters. With the nozzle radius R_n replaced by the liquid bridge's neck radius R, we have the Bond number $\mathrm{Bo} = \rho g R^2/\sigma$. With U the characteristic velocity and η_0 the zero-shear viscosity of the viscoelastic fluid, the Reynolds number $\mathrm{Re} = \rho U R/\eta_0$ characterizes the relative importance of inertial and viscous stresses. With λ the characteristic relaxation time of the viscoelastic fluid, the Weissenberg number $\mathrm{Wi} = \lambda U/R$ characterizes the relative importance of elastic and viscous stresses. Finally, the capillary number $\mathrm{Ca} = \eta_0 U/\sigma$ characterizes the relative importance of viscous and capillary stresses (1). For H close to H_c where $\mathrm{Bo} > 1$, thinning of the liquid bridge is dominated by slow gravitational drainage (8). To speed up the process, the mainstream industrial approach is to retract the nozzle to a distance $H \gg H_c$ (9) such that the liquid bridge thins with an initial radius $R \ll R_n$ (Fig. 1*B*). As the Bond number $\mathrm{Bo} \ll 1$, a Newtonian liquid bridge will enter the visco-capillary regime and thin linearly in time with a speed proportional to the capillary velocity $v_{cap} \equiv \sigma/\eta_0$ (10). For a typical $\eta_0 = 60$ Pa·s, $\sigma = 20$ mN/m, and $R = 0.5$ mm, the liquid bridge breakup takes $\mathcal{O}(10$ s). On the other hand, a viscoelastic liquid bridge will enter the elasto-capillary regime. Elastic stresses induced as the bridge thins can retard the thinning process, causing the liquid bridge radius to decay exponentially with time constant $(3\lambda)^{-1}$ and a front factor that depends on the elasto-capillary number $\mathrm{Ec} \equiv \mathrm{Wi/Ca} = \lambda\sigma/\eta_0 R$ (11).

Nozzle retraction can speed up the dispensing process; however, it also reduces the precision as the satellite droplets (4) and long capillary tails (12) formed after pinch-off may fall randomly and contaminate the substrate (Fig. 1*C*). This speed–precision trade-off problem motivates seeking alternative methods to destabilize viscoelastic liquid bridges and decrease the time to pinch-off. While many studies have considered how extension can destabilize liquid bridges due to its applications in rheology (1) and printing (13), none of them have considered torsion, i.e., steadily rotating one end of the liquid bridge while keeping the other end fixed (Fig. 1*D*). Here, we explore how torsion may destabilize viscoelastic liquid bridges and decrease the time to pinch-off. We show that even viscoelastic bridges with $H < H_c$, which would never break under the action of gravity and capillarity alone, can be broken in $\mathcal{O}(1$ s) by applying torsion. By high-speed video analysis and viscoelastic flow simulation, we identify that the mechanism behind such effective breakup

Significance

Dispensing of viscoelastic fluids is common in applications like electronic packaging, food engineering, and additive manufacturing. However, viscoelasticity leads to problems like slow liquid bridge breakup, stringiness, and satellite droplets generation. By high-speed imaging and numerical simulation, we show that torsion can break short, capillary stable liquid bridges in the order of 1 s. The underlying mechanism is edge fracture, an often undesired viscoelastic flow instability characterized by the sudden indentation of the fluid's free surface when the fluid is subjected to shear. Our study represents an attempt to take advantage of edge fracture to benefit practical applications, potentially leading to improved fluid dispensing protocols.

Author contributions: S.T.C. and H.A.F. conceived the study; S.T.C. performed experiments; F.P.A.v.B. performed simulations; H.A.F. contributed data analysis tools; S.T.C., F.P.A.v.B., H.A.F., A.M., S.J.H., P.D.A., and A.Q.S. analyzed data; S.T.C., F.P.A.v.B., H.A.F., A.M., S.J.H., P.D.A., and A.Q.S. wrote the paper; S.T.C. and A.M. performed rheological characterizations; and S.J.H., P.D.A., and A.Q.S. supervised research.

The authors declare no competing interest.

This article is a PNAS Direct Submission.

This open access article is distributed under Creative Commons Attribution-NonCommercial-NoDerivatives License 4.0 (CC BY-NC-ND).

[1]S.T.C., F.P.A.v.B., and H.A.F. contributed equally to this work.

[2]To whom correspondence may be addressed. Email: amy.shen@oist.jp.

This article contains supporting information online at https://www.pnas.org/lookup/suppl/doi:10.1073/pnas.2104790118/-/DCSupplemental.

Published June 11, 2021.

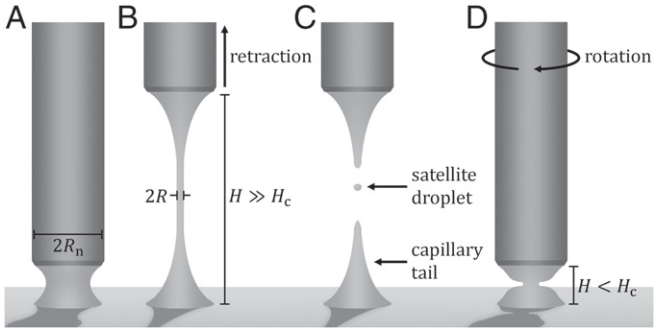

Fig. 1. A typical dispensing process. (*A*) A liquid bridge of height H connecting the nozzle of radius R_n and the substrate. (*B*) Retracting the nozzle to a height $H \gg H_c$ above the critical height H_c destabilizes the liquid bridge and causes it to thin under surface tension (7, 8). (*C*) For viscoelastic liquid bridges, nozzle retraction creates satellite droplets and a long capillary tail, which may contaminate the substrate. (*D*) By applying torsion to a stable viscoelastic liquid bridge, an indent propagates toward the bridge center, leading to breakup even at $H < H_c$.

is edge fracture, a viscoelastic flow instability characterized by the sudden indentation of the fluid's free surface above a critical shear rate (14–20). Edge fracture causes the radius evolution in time $R(t)$ of viscoelastic bridges to undergo power-law decay. With Ω the angular speed of the steady rotation applied on one end of the liquid bridge, such power-law decay is solely governed the dimensionless Tanner number $\mathrm{Tn} \equiv \mathrm{WiCa} = \lambda\eta_0 R\Omega^2/\sigma$, introduced in this work, which characterizes the relative importance of normal and capillary stresses.

Preliminaries

The dynamics of viscoelastic liquid bridges under torsion depend on the complex interaction between inertial, elastic, capillary, and gravitational stresses (1, 21), which involves four dimensionless parameters: the Reynolds number Re, the Weissenberg number Wi, the capillary number Ca, and the Bond number Bo. To simplify the problem, we consider an axisymmetric model system consisting of a liquid bridge contained by surface tension between two coaxial circular plates with radius $R_p = 2.85$ mm (Fig. 2*A*). The upper plate can rotate unidirectionally and the lower plate can be translated vertically. A droplet of volume 40 μL is injected between the two plates with an initial separation $H_0 = 2.5$ mm and then stretched to a final separation $H \leq 7$ mm at a rate of 0.67 mm/s. When H is reached, the upper plate is angularly accelerated to a rotational rate f (or angular speed $\Omega = 2\pi f$) within a timespan $t_f \approx 1$ s, high-speed video is captured, and the neck radius R of the liquid bridge is tracked over time t. To investigate inertial and elastic effects separately, two types of fluids are used. The first type is a Newtonian fluid (Infineum S1054), which is a low-molecular-weight polyisobutylene commonly used as a Newtonian solvent due to its nonvolatile nature and high viscosity (4, 22–25). Infineum S1054 has density $\rho = 888$ kg/m^3, surface tension $\sigma = 31.5$ mN/m, and viscosity $\eta \equiv \eta_0 = 27$ Pa·s. The second type is a viscoelastic fluid (silicone oil) with density $\rho = 970$ kg/m^3 and surface tension $\sigma = 20.6$ mN/m. Its rheology can be fitted by the Giesekus model (Fig. 2 *B*–*D*), which is able to describe shear thinning, variable first- and second-normal stress differences N_1 and N_2, and nonlinear time effects (26–28). The Giesekus model has been successfully used to model wormlike micellar solutions (29–32) and polymer fluids (33) and has been used extensively for numerical simulations of viscoelastic flows (24, 34–37). A single-mode Giesekus model contains two linear parameters (η_0, λ) and a nonlinear mobility parameter α, which represents the anisotropy of hydrodynamic drag on a polymer molecule. The value of α affects the magnitude of N_2 and the degree of shear thinning (38). For $\alpha = 0$, neither N_2 nor shear thinning is present. Superposing several single-mode models gives the multimode Giesekus model (24), which for polymer melts takes the form

$$\boldsymbol{\tau} = \sum\nolimits_{i=1}^{N} \boldsymbol{\tau}_i, \qquad [1]$$

$$\lambda_i \left(\partial_t \boldsymbol{\tau}_i + \boldsymbol{v}\cdot\nabla\boldsymbol{\tau}_i - \nabla\boldsymbol{v}^{\mathrm{T}}\cdot\boldsymbol{\tau}_i - \boldsymbol{\tau}_i\cdot\nabla\boldsymbol{v}\right) + \boldsymbol{\tau}_i + \frac{\alpha_i\lambda_i}{\eta_i}\boldsymbol{\tau}_i^2 = 2\eta_i\boldsymbol{D}, \qquad [2]$$

with $\boldsymbol{v}$ the velocity vector; $\boldsymbol{\tau}$ the viscoelastic stress tensor; $\boldsymbol{D} = \frac{1}{2}(\nabla\boldsymbol{v} + \nabla\boldsymbol{v}^{\mathrm{T}})$ the deformation rate tensor; N the number of modes; and $\boldsymbol{\tau}_i$, η_i, λ_i, and α_i the viscoelastic stress tensor, polymer viscosity, relaxation time, and mobility parameter of the ith mode, respectively. A three-mode Giesekus model with $\eta_i = 38, 8, 12.6$ Pa·s, $\lambda_i = 5, 0.8, 0.3$ ms, and a single $\alpha_i = \alpha = 0.49$ led to the best fit of the measured rheological data. The zero-shear viscosity is $\eta_0 = \sum_i \eta_i = 58.6$ Pa·s. An average relaxation time $\bar{\lambda}$ (24) is defined as $\bar{\lambda} = \sum_i \eta_i\lambda_i/\eta_0 = 3.42$ ms. Fig. 2*B* shows that the three-mode Giesekus model fit (line) agrees well with the small-amplitude oscillatory shear (SAOS) measurement results (symbols) of the silicone oil. Fig. 2 *C* and *D* further shows that the normal stress differences predicted by the three-mode Giesekus model (lines) agree well with the steady-shear measurement results (symbols). Dividing the first- and second-normal stress differences N_1 and N_2 by $\dot{\gamma}^2$ gives the normal stress coefficients $\Psi_1(\dot{\gamma})$ and $\Psi_2(\dot{\gamma})$. For $\dot{\gamma} < 100\ \mathrm{s}^{-1}$ where $N_1, N_2 \propto \dot{\gamma}^2$, the zero-shear normal stress coefficients are $\Psi_{1,0} = 0.42$ Pa·s^2 and $\Psi_{2,0} = 0.1$ Pa·s^2.

To further simplify the problem, we use dimensional analysis to identify which balance of stresses dominates the liquid bridge thinning process. For the model system (Fig. 2*A*), the characteristic velocity is $U = R\Omega$. The Reynolds number, Weissenberg number, capillary number, and Bond number can be expressed as $\mathrm{Re} = \rho R^2\Omega/\eta_0$, $\mathrm{Wi} = \bar{\lambda}\Omega$, $\mathrm{Ca} = \eta_0 R\Omega/\sigma$, and $\mathrm{Bo} = \rho g R^2/\sigma$. For the Newtonian Infineum S1054 fluid, thinning of the

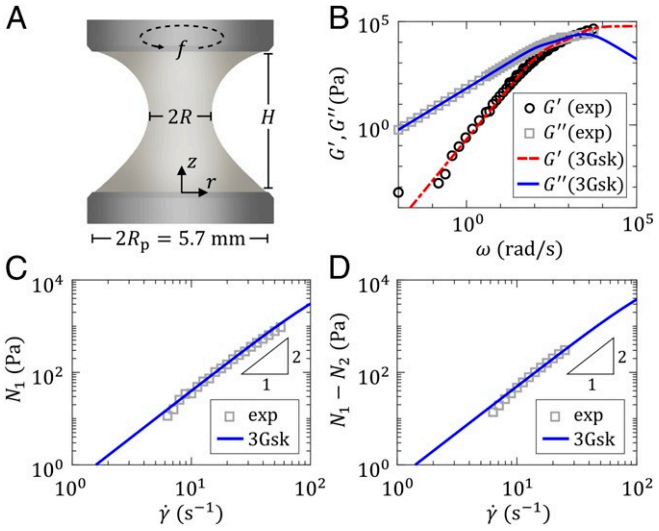

Fig. 2. (*A*) The experimental setup that consists of a liquid bridge between two concentric plates of radius $R_p = 2.85$ mm. The upper plate can unidirectionally rotate at a rate of f to apply torsion on the liquid bridge and the lower plate can move vertically. (*B*) Storage and loss modulus G' and G''. (*C*) First normal stress difference N_1. (*D*) Difference between the first- and second-normal stress differences $N_1 - N_2$, of the viscoelastic liquid bridge material. Symbols denote experimental measurements; lines denote predictions of the three-mode Giesekus model.

liquid bridge is characterized by Re, Ca, and Bo. With a typical radius $R = 1$ mm and rotational rate $f = 30$ Hz, one obtains $\mathrm{Re} \in \mathcal{O}(10^{-2})$, $\mathrm{Bo} \in \mathcal{O}(10^{-1})$, and $\mathrm{Ca} \in \mathcal{O}(10^{2})$. The number of parameters can be reduced by introducing the Weber number $\mathrm{We} \equiv \mathrm{ReCa} = \rho R^3 \Omega^2/\sigma$ and the inverse-squared Ohnesorge number $\mathrm{Oh}^{-2} \equiv \mathrm{Re/Ca} = \rho\sigma R/\eta_0^2$. The Weber number We characterizes the relative importance of centrifugal and capillary stresses. The inverse-squared Ohnesorge number Oh^{-2} characterizes the combined importance of inertial and capillary stresses compared to viscous stress. Essentially, the pair $\{\mathrm{We}, \mathrm{Oh}^{-2}\}$ contains the same information as $\{\mathrm{Re}, \mathrm{Ca}\}$. However, since $\mathrm{Oh}^{-2} \in \mathcal{O}(10^{-5})$ is much smaller than both

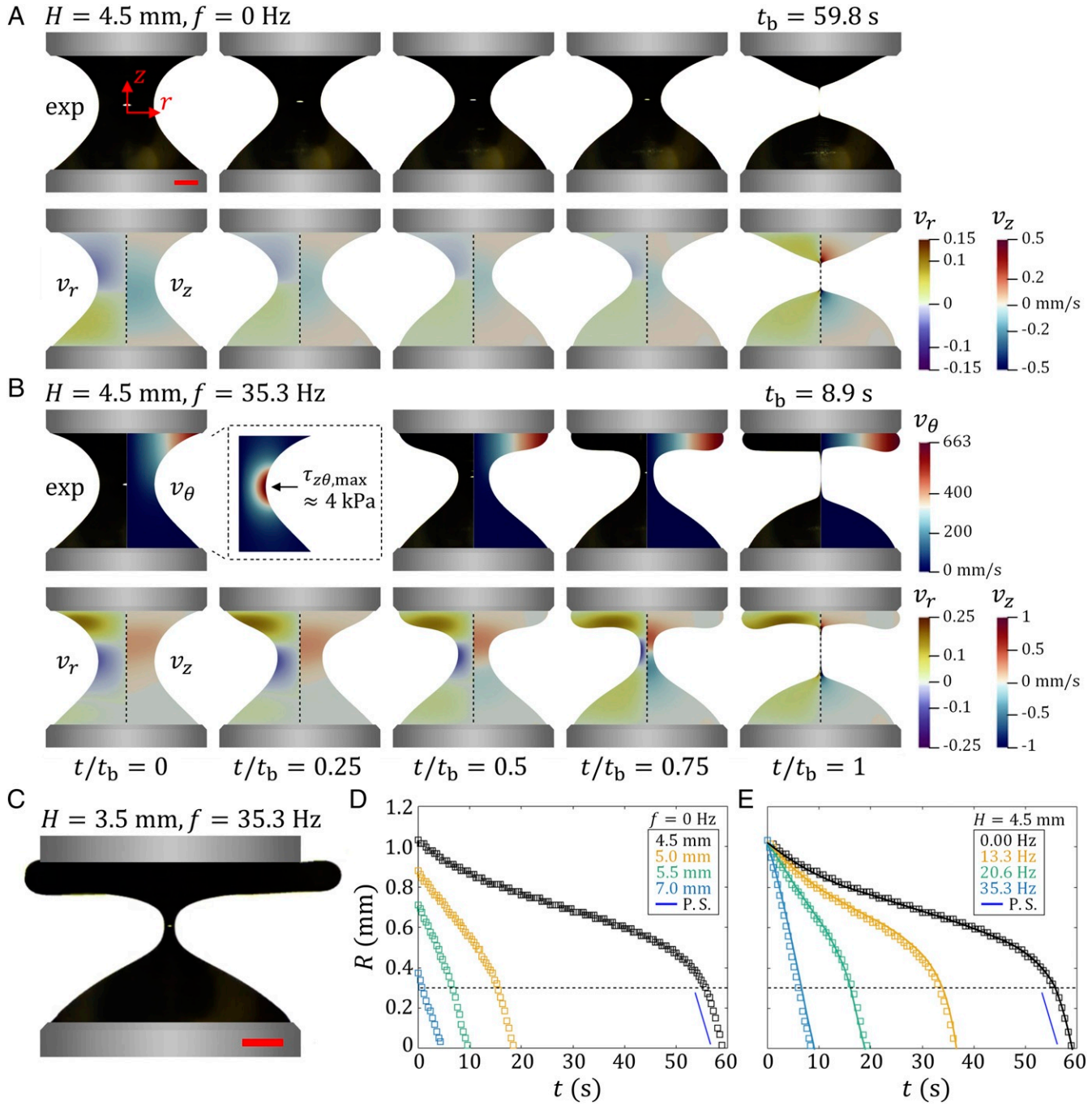

Fig. 3. Experiment and simulation of liquid bridge breakup dynamics of the Newtonian Infineum S1054 fluid. (*A*) A liquid bridge of $H = 4.5$ mm breaking up under capillary action and gravity only. *Upper* row shows the experimental images; *Lower* row shows the simulated radial and axial velocity fields v_r (left-hand side [L.H.S.]) and v_z (right-hand side [R.H.S.]). (Scale bar: 1 mm.) (*B*) A liquid bridge of $H = 4.5$ mm breaking up with a rotational rate $f = 35.3$ Hz. *Upper* row shows a combination of experimental images (L.H.S.) and simulated azimuthal velocity field v_θ (R.H.S.). *Lower* row shows the simulated radial and axial velocity fields v_r (L.H.S.) and v_z (R.H.S.). *Inset* dotted box shows that shear stress $\tau_{z\theta}$ is localized around the liquid bridge's neck and has a maximum value of around 4 kPa. (*C*) Experimental image of a liquid bridge of $H = 3.5$ mm breaking up with a rotational rate $f = 35.3$ Hz, whose upper portion is spinning off of the plate. (Scale bar: 1 mm.) See Movies S1–S3 for videos that correspond to *A*–*C*. (*D*) Radius evolution $R(t)$ of liquid bridges of different plate separations H with no rotation applied. (*E*) Radius evolution $R(t)$ of liquid bridges of $H = 4.5$ mm under different rotational rates f. Symbols denote experimental measurements; solid lines denote numerical predictions by the Newtonian model. P. S. denotes the Papageorgiou similarity solution.

Bo $\in \mathcal{O}(10^{-1})$ and We $\in \mathcal{O}(1)$, the contribution from Oh^{-2} to the liquid bridge thinning can be neglected. Hence, the number of dimensionless parameters needed to characterize thinning of the Newtonian liquid bridge is effectively reduced from three to two. Also, unlike {Re, Ca} where both parameters depend on the rotational rate f, only We depends on f for {We, Oh^{-2}}. Using {We, Oh^{-2}} instead of {Re, Ca} thus allows us to interpret the effect of varying f more easily and in a physically more meaningful way. Following a similar logic, for the viscoelastic silicone oil, thinning of the liquid bridge is characterized by Re, Wi, Ca, and Bo. For $R = 1$ mm and $f = 30$ Hz, the effect of Re $\in \mathcal{O}(10^{-3})$ is negligible compared to that of Wi $\in \mathcal{O}(10^{-1})$, Bo $\in \mathcal{O}(10^{-1})$, and Ca $\in \mathcal{O}(10^{2})$. The number of parameters can be further reduced by introducing the Tanner number Tn $\equiv$ WiCa $= \bar{\lambda}\eta_0 R\Omega^2/\sigma$ and the elasto-capillary number Ec $\equiv$ Wi/Ca $= \bar{\lambda}\sigma/\eta_0 R$. The Tanner number Tn characterizes the relative importance of normal stresses (as $\Psi_{1,0}, \Psi_{2,0} \propto \bar{\lambda}\eta_0$) and capillary stress. The elasto-capillary number Ec characterizes the combined importance of elastic and capillary stresses compared to viscous stress. As Ec $\in \mathcal{O}(10^{-3})$ is much smaller than both Tn $\in \mathcal{O}(10^{2})$ and Bo $\in \mathcal{O}(10^{-1})$, the effect of Ec can be neglected. Thus, the number of dimensionless

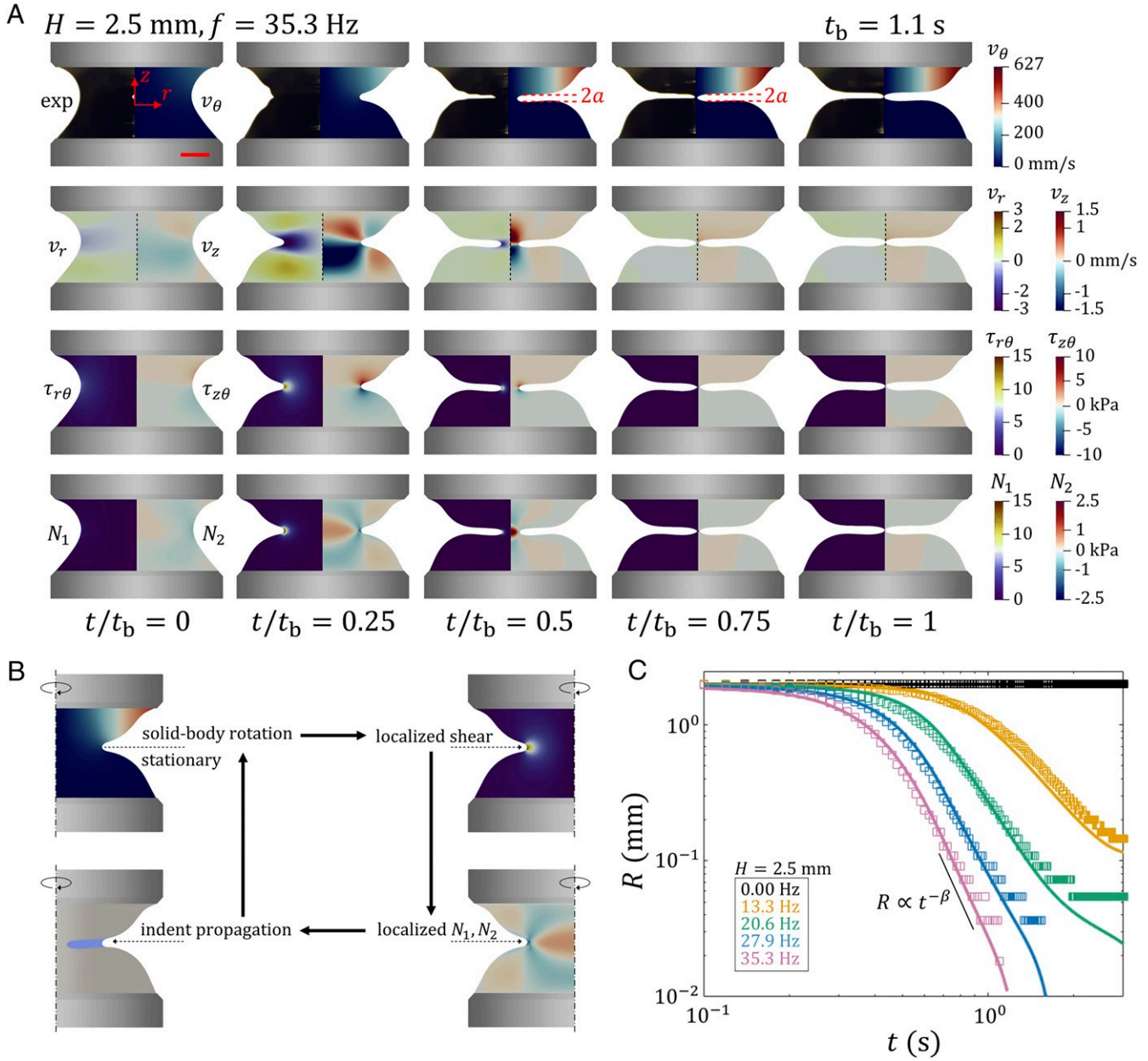

Fig. 4. Experiment and simulation of liquid bridge breakup dynamics of the viscoelastic silicone oil. (*A*) A liquid bridge of $H = 2.5$ mm breaking up with a rotational rate $f = 35.3$ Hz. *Top* row shows a combination of experimental images (L.H.S.) and simulated azimuthal velocity field v_θ (R.H.S.). *Upper Middle* row shows the simulated radial and axial velocity fields v_r (L.H.S.) and v_z (R.H.S.). *Lower Middle* row shows the simulated shear stress fields $\tau_{z\theta}$ (L.H.S.) and $\tau_{r\theta}$ (R.H.S.). *Bottom* row shows the simulated distributions of the first-normal stress difference $N_1 = \tau_{\theta\theta} - \tau_{zz}$ (L.H.S.) and second-normal stress difference $N_2 = \tau_{zz} - \tau_{rr}$ (R.H.S.). In the breakup process, an indentation of size a forms and propagates toward the axis of rotation. (Scale bar: 1 mm.) See Movie S4 for the corresponding video to *A*. (*B*) A flowchart explaining the observations in *A*. (*C*) Radius evolution $R(t)$ of liquid bridges of $H = 2.5$ mm under different rotational rates f. Symbols denote experimental measurements; solid lines denote numerical predictions by the three-mode Giesekus model.

parameters needed to characterize thinning of the viscoelastic liquid bridge is reduced from four to two. As a side note, if the normal stress component that governs the liquid bridge thinning process is known a priori, the term $\bar{\lambda}\eta_0$ in Tn may be replaced by either $\Psi_{1,0}$ or $\Psi_{2,0}$. However, since the governing normal stress component is presently unknown, we shall stick to the current definition of Tn throughout this paper.

Results

Newtonian Liquid Bridges under Torsion. Having the dominant balance of stresses identified, we now consider how Newtonian liquid bridges behave under torsion. Fig. 3 *A* and *B* shows the experimental liquid bridge configurations and the corresponding simulated azimuthal, radial, and vertical velocities (v_θ, v_r, v_z) of the Infineum S1054 fluid at different times t with a fixed plate separation $H = 4.5$ mm. Without plate rotation (Fig. 3*A* and Movie S1), gravity induces a region of negative axial velocity v_z around the liquid bridge's neck. This transfers fluid downward as shown by the negative radial velocity v_r at the top plate and leads to the subsequent breakup at $t_b = 59.8$ s. Meanwhile, with a rotational rate of $f = 35.3$ Hz (Fig. 3*B* and Movie S2), the centrifugal force associated with the azimuthal velocity v_θ spreads fluid outward in the radial direction, rendering v_r positive near the top plate and flattening the upper portion of the liquid bridge into a pancake shape. This transfers fluid upward as shown by the positive v_z around the liquid bridge's neck and leads to breakup at $t_b = 8.9$ s. During the thinning process, as the liquid bridge surface is concave, v_θ concentrates around the rim of the upper rotating plate. The magnitude of v_θ decreases linearly toward the axis of rotation, meaning that the upper portion of the liquid bridge is rotating like a solid body. On the other hand, the lower portion of the liquid bridge is almost stationary. Such speed difference between the upper and lower portions localizes shear around the liquid bridge's neck (Fig. 3 *B*, *Inset* dashed box). Hence, we can conclude that localized shear is possible even for a Newtonian fluid as long as the free surface of the liquid bridge is concave. Decreasing the plate separation to $H = 3.5$ mm renders the liquid bridge stable to capillarity and gravity. Applying a rotational rate of $f = 35.3$ Hz, the induced centrifugal force would cause fluids to spin off the upper plate radially outward prior to pinch-off (Fig. 3*C* and Movie S3). In Fig. 3 *D* and *E*, we plot the neck radius R as a function of time t at different plate separations H and rotational rates f. Without plate rotation (Fig. 3*D*), the breakup time decreases for increasing H. With a fixed plate separation $H = 4.5$ mm (Fig. 3*E*), the breakup time decreases for increasing f. In both cases, the thinning speed $\dot{R}$ approaches the Papageorgiou similarity solution $\dot{R}_{PS} = -0.0709\sigma/\eta_0$ (10) for $R < 0.3$ mm (blue lines in Fig. 3 *D* and *E*), which corresponds to a Weber number $We < 0.04$ (for $f \leq 35.3$ Hz) and a Bond number $Bo < 0.025$. This signifies that when R is small enough, the thinning dynamics of a Newtonian liquid bridge is governed solely by a balance of the capillary and viscous forces.

Viscoelastic Liquid Bridges under Torsion. With the effect of torsion to Newtonian liquid bridges investigated, we can identify the elastic effect by comparing data obtained from a viscoelastic fluid to those from a Newtonian fluid. Fig. 4*A* shows the experimental liquid bridge configurations; simulated azimuthal, radial, and vertical velocities (v_θ, v_r, v_z); first- and second-normal stress differences ($N_1 = \tau_{\theta\theta} - \tau_{zz}$, $N_2 = \tau_{zz} - \tau_{rr}$); and two of the shear stress components ($\tau_{z\theta}$, $\tau_{r\theta}$) of the viscoelastic silicone oil subjected to a $f = 35.3$-Hz plate rotation at different times t with a fixed plate separation $H = 2.5$ mm. Under such small separation, the liquid bridge is stable to the action of surface tension and gravity; it never undergoes breakup without plate rotation. Once rotation is applied, as in the Newtonian case, the concave surface of the liquid bridge renders the upper portion rotating like a solid body and the lower portion rather stationary, localizing shear around the liquid bridge's neck (*SI Appendix*, Fig. S1). However, unlike Newtonian fluids, viscoelastic fluids can generate normal stresses when subjected to shear as described by the Giesekus model (26–28). Thus, a localized region of positive first-normal stress difference N_1 and negative second-normal stress difference N_2 is induced, which in turn curves the surface and localizes shear even further. Such feedback results in the formation of an indent of size $2a \approx 0.2$ mm (Fig. 4*A* and Movie S4) at the neck, which propagates toward the axis of rotation, leading to breakup at $t_b = 1.1$ s. The aforementioned indent propagation mechanism is summarized into a flowchart as shown in Fig. 4*B*. We note that the indent size $2a$ is an order of magnitude smaller than the capillary length $l_{cap} = \sqrt{\sigma/\rho g} \approx 1.5$ mm. Hence, gravity can be neglected, implying that the thinning of the viscoelastic liquid bridge by torsion is governed solely by the Tanner number $\mathrm{Tn} = \bar{\lambda}\eta_0 R\Omega^2/\sigma$. We also note that the breakup time t_b is comparable to the time $t_f \approx 1$ s for the upper plate to reach $f = 35.3$ Hz. Therefore, during indent propagation the rotational rate is not constant but increases monotonically with time. Fig. 4*C* shows the radius evolution $R(t)$ of the liquid bridge subjected to different rotational rates f. Without plate rotation ($f = 0$ Hz), the radius $R(t)$ is a constant as the liquid bridge is stable. When rotation is applied, the radius shows power-law decay $R \propto t^{-\beta}$. The power-index β increases with increasing f. For $f \leq 20.6$ Hz, such power-law decay occurs for $t > t_f \approx 1$ s. Also, for $f = 35.3$ Hz, decreasing t_f in the simulation, such power-law decay can still be observed (*SI Appendix*, Fig. S2). Hence, it is not a mere coincidence caused by the finite t_f but an intrinsic feature of the indent propagation process. If we assume the silicone oil to be Newtonian in the simulation, applying rotation essentially has no effect on the liquid bridge during the timespan considered; $R(t)$ is constant in Fig. 4*C* just like the $f = 0$-Hz case. This provides further evidence that the indent propagation observed in this work is a normal stress effect.

Edge Fracture. Knowing that the indentation observed is a normal stress effect, next we ask which normal stress difference is governing the process. In fact, the indentation process and flow patterns that we have described for the viscoelastic liquid bridges closely resemble edge fracture. Edge fracture is a flow instability often observed when a viscoelastic fluid is sheared at above a critical shear rate in a cone-plate or parallel-plate rheometer fixture. The instability is characterized by the formation of an indent on the fluid's free surface (14–20), which can localize shear around its tip and induce apparent shear bands that invade into the fluid bulk (16, 19). In an insightful early study (14), by assuming a semicircular indent of radius a on the free surface of a second-order fluid sheared between two semi-infinite parallel plates separated by a distance $H \gg a$, Tanner and Keentok (14) derived a criterion $|N_2| > 2\sigma/3a$ for edge fracture. When the criterion is satisfied, the second-normal stress difference at the indent tip $N_{2,tip}$ overcomes the Laplace pressure $p_L = \sigma/a$ and leads to indent formation. Lee et al. (17) then performed a series of experiments using fluids with different normal stress ratios $-N_2/N_1$. Their results confirmed Tanner and Keentok's (14) proposition that edge fracture is controlled by N_2 but not by N_1. Subsequently, Huilgol et al. (18) deduced that the stress normal to the semicircular indent surface assumed by Tanner and Keentok (14) is tensile, which will tend to deepen the indent. They also argued that as the indent propagates and its surface becomes parallel to the propagation direction, an outward normal stress will act on the indent's upper and lower flat surfaces. Such outward normal stress is compressive to the indent; hence, it will tend to close the indent and may prevent the indent from propagating further. Then, by assuming a rectangular indent of width $2a$ and depth c, Keentok and Xue (15) simulated the shearing viscoelastic flow between two parallel

ENGINEERING

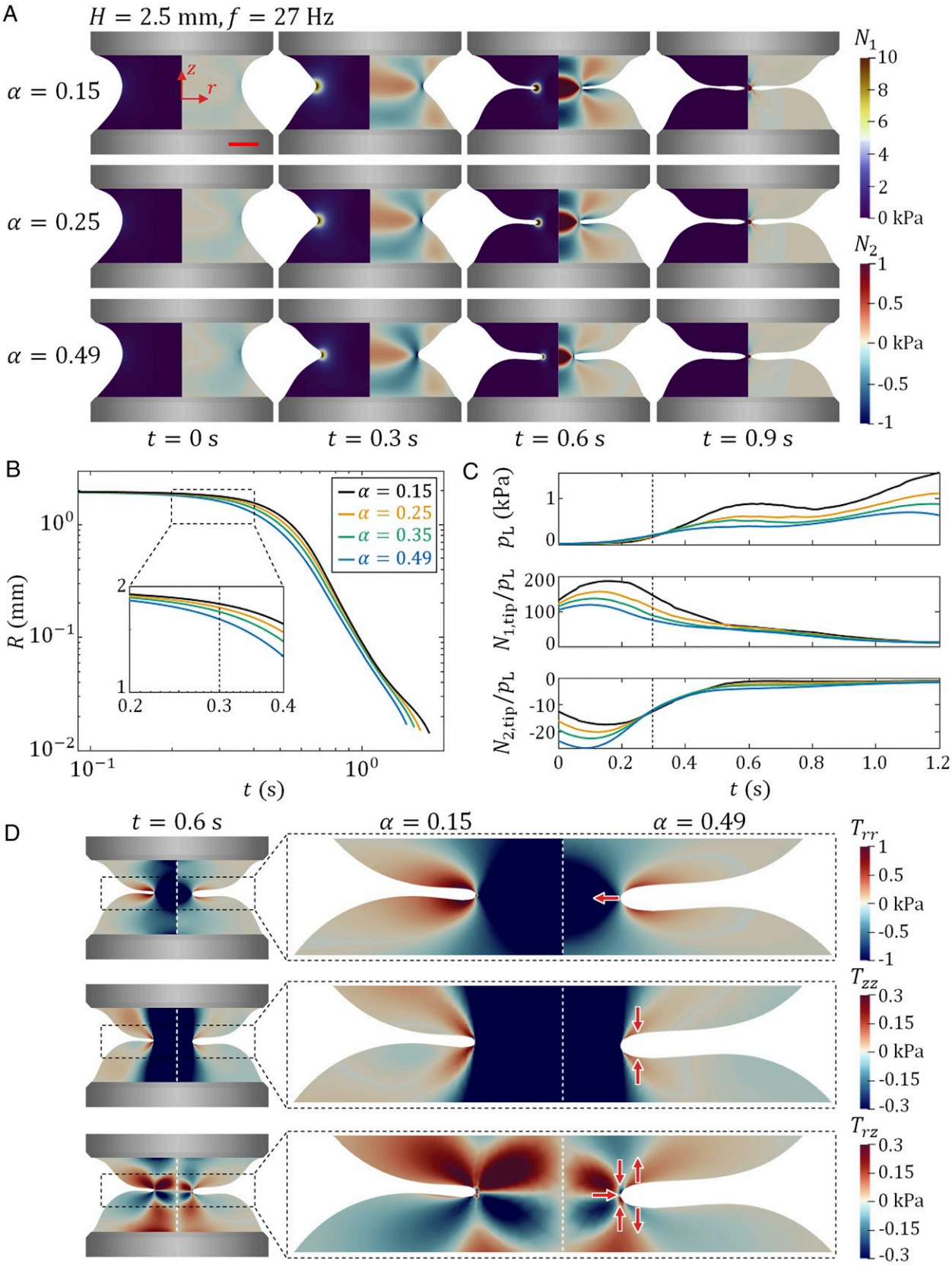

Fig. 5. Effect of the mobility parameter α on the breakup dynamics of viscoelastic liquid bridges with $H = 2.5$ mm and subjected to a plate rotational rate of $f = 27$ Hz. (*A*) Simulated distributions of the first-normal stress difference $N_1 = \tau_{\theta\theta} - \tau_{zz}$ (L.H.S.) and second-normal stress difference $N_2 = \tau_{zz} - \tau_{rr}$ (R.H.S.) of liquid bridges with $\alpha = 0.15$, 0.25, and 0.49. (Scale bar: 1 mm.) (*B*) Simulated radius evolution $R(t)$ of liquid bridges with different α. (*C*) Time evolution of the Laplace pressure p_L and normal stress differences $N_{1,tip}$ and $N_{2,tip}$ at the indent tip with different α. Here, $N_{1,tip}$ and $N_{2,tip}$ are both normalized by p_L. (*D*) Simulated distributions of the total stress tensor components $T_{rr} = -p + \tau_{rr}$ (*Top*), $T_{zz} = -p + \tau_{zz}$ (*Middle*), and $T_{rz} = \tau_{rz}$ (*Bottom*) of liquid bridges with $\alpha = 0.15$ and 0.49 at $t = 0.6$ s. Red arrows indicate direction of the stress acting on the surface. For clarity, only the arrows for $\alpha = 0.49$ are shown.

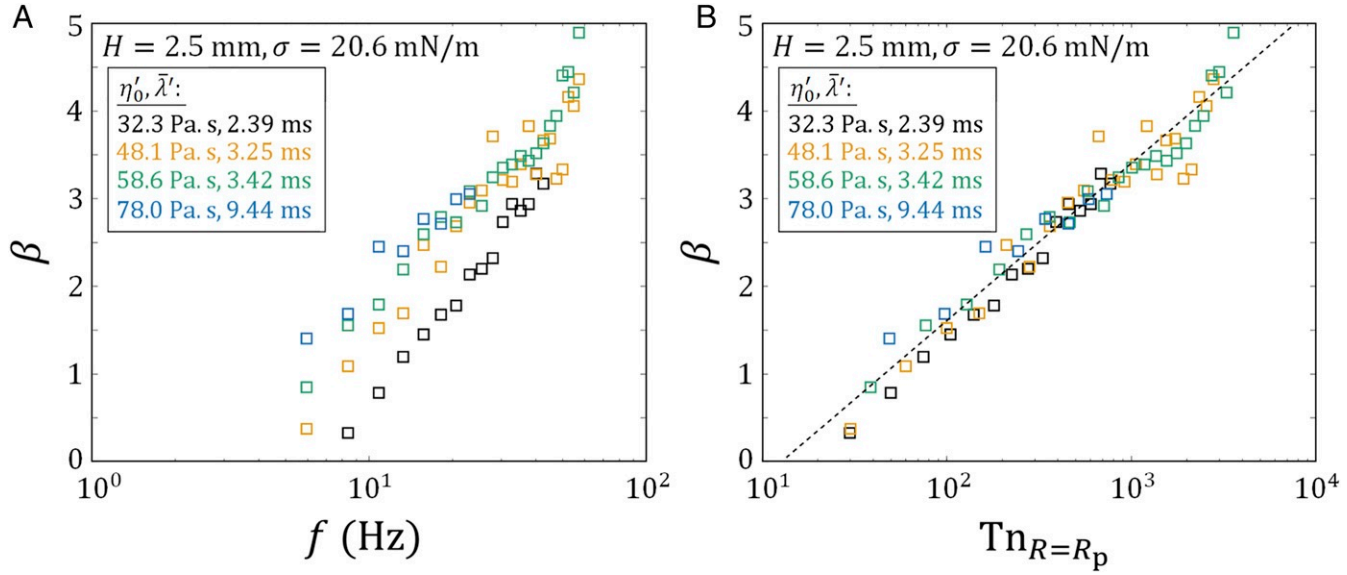

Fig. 6. Experimentally measured best-fit power-law index β of the radius evolution $R(t) \propto t^{-\beta}$ of different viscoelastic silicone oil liquid bridges with $H =$ 2.5 mm and surface tension $\sigma = 20.6$ mN/m. Each color represents one of the four silicone oils with different viscosities η_0' and average relaxation times $\bar{\lambda}'$. (*A*) The power-law index β as a function of the plate rotational rate f. (*B*) The power-law index β as a function of the Tanner number $\mathrm{Tn}_{R=R_p} = \bar{\lambda}' \eta_0' R_p \Omega^2 / \sigma$. The dotted line $\beta = 0.78 \ln(\mathrm{Tn}) - 2$ is a visual guidance for showing the data collapse.

plates using the Phan–Thien–Tanner model (39). Although the meniscus of the fluid was not modeled as a free surface, their obtained normal stress distributions around the indent surface agreed with the analysis of Huilgol et al. (18). More recently, Hemingway and Fielding (16) performed a linear stability analysis using both the Johnson–Segalman model (40) and the Giesekus model (26, 27). They derived an onset criterion for edge fracture, which extended the Tanner–Keentok criterion. In particular, they provided insight that shear stress may also contribute to edge fracture by counteracting the effects of N_2. Later, they showed that precursors to edge fracture can induce quasi-bulk shear banding, which can also induce edge fracture (19).

If the indentation process that we have observed is indeed caused by edge fracture, it should demonstrate three defining characteristics. First, based on the analysis of Tanner and Keentok (14), the indent formation process should be driven by N_2 but not by N_1. Second, based on the analysis of Huilgol et al. (18), there should be a tensile normal stress that acts on the indent tip and a compressive normal stress that acts on the indent's flat surfaces. Third, based on the analysis of Hemingway and Fielding (16), the shear stress (τ_{rz} in our case) should counteract the effects of N_2. To test these, we systematically vary the mobility parameter α in the simulation and see how it affects the thinning dynamics of the viscoelastic liquid bridge subjected to a rotational rate of $f = 27$ Hz. Fig. 5*A* shows the simulated liquid bridge configurations for $\alpha = 0.15$, 0.25, and 0.49. Distributions of the first- and second-normal stress differences N_1 and N_2 are also shown (left-hand side [L.H.S.] and right-hand side [R.H.S.], respectively). For a lower value of α, the indent is sharper. It also propagates more slowly, although the effect is minor. For instance, at $t = 0.3$ and 0.6 s, the indent of $\alpha = 0.49$ precedes that of $\alpha = 0.15$ and 0.25, which catch up at $t = 0.9$ s. For a lower value of α, the magnitude of N_1 is seen to be larger at the indent tip at all times. At $t = 0.3$ s when the indent just starts to form, the magnitude of the negative N_2 is seen to be smaller at the indent tip; while at $t = 0.6$ s when the indent is formed, it is larger on the whole indent surface. For all values of α, N_1 is concentrated only around the indent tip and N_2 is distributed on the whole indent surface. Hence, N_2 is the only possible normal stress difference that can act on the indent surface away from the tip and hence shape the indent. Fig. 5*B* shows the radius evolution $R(t)$ of the liquid bridges for different values of α. For lower values of α, breakup time of the liquid bridge is longer. This indicates a lower magnitude of normal stress difference, which governs the indent formation process. Fig. 5*C* further shows the time evolution of the Laplace pressure p_L and normal stress differences $N_{1,\mathrm{tip}}$, $N_{2,\mathrm{tip}}$ at the indent tip for different α. For $t \leq 0.3$ s, when the indent just starts to form, the curves of p_L for different α overlap. This signifies that the liquid bridges with different α have similar shapes and thus similar shear rate at the indent tip for $t \leq 0.3$ s. Therefore, we can compare the magnitudes of $N_{1,\mathrm{tip}}$ and $N_{2,\mathrm{tip}}$ for different α. Here, a lower value of α leads to a higher magnitude of $N_{1,\mathrm{tip}}/p_L$ and a lower magnitude of $N_{2,\mathrm{tip}}/p_L$. Hence, the indent formation process is governed by the second-normal stress difference N_2. With p the pressure in the liquid bridge, Fig. 5*D* shows the radial, vertical, and shear components $T_{rr} = -p + \tau_{rr}$, $T_{zz} = -p + \tau_{zz}$, and $T_{rz} = \tau_{rz}$ of the total stress tensor for $\alpha = 0.15$ and 0.49 at $t =$ 0.6 s. For both values of α, the indent is surrounded by a positive T_{rr}, which indicates that the radial normal stress acting on the indent tip is indeed tensile. Such tensile stress pulls the indent radially inward toward the liquid bridge center and propagates the indent. The indent is also surrounded by a positive T_{zz} except at the indent tip. This indicates that T_{zz} is compressive to the indent; it pulls the upper and lower surfaces of the indent toward each other. As the upper and lower surfaces both become flat, the Laplace pressure there will essentially be zero. This leads us to question which stress is keeping the surfaces flat and stopping T_{zz} from further compressing the indent. The only stress that can do so is the shear stress T_{rz}. Away from the indent tip close to the flat surfaces, T_{rz} is positive in the upper portion and negative in the lower portion of the liquid bridge. If there is any area on the indent surface that is not horizontal, then there will be a vertical component of T_{rz} induced, which tends to make the surface horizontal. Depending on the horizontalness of the surface, T_{rz} can counteract T_{zz}. This explains why all indents observed tend to have horizontal flat surfaces while propagating. Close to the indent tip, T_{rz} is negative above and positive below the tip. As the surface of the indent tip is curved, there is a vertical component of T_{rz} that compresses the indent just like T_{zz}; also, there is a horizontal component that counteracts the tensile T_{rr}. Our analysis of Fig. 5 above

shows that the indentation process we observe in the viscoelastic liquid bridges actually demonstrates the three defining characteristics of edge fracture. This provides strong evidence to conclude that the indentation process is indeed caused by edge fracture. It also suggests that the normal stress effect that the Tanner number Tn characterizes is N_2.

Dynamic Similarity of Edge Fracture. To verify that the indent propagation is solely governed by the Tanner number $\mathrm{Tn} = \bar{\lambda}\eta_0 R\Omega^2/\sigma$, we now show that the power-law decay of $R(t)$ has the same slope as long as Tn is the same. As the first step, we analyze high-speed videos obtained from liquid bridges of three additional silicone oils. These silicone oils have the same surface tension $\sigma' = \sigma = 20.6$ mN/m

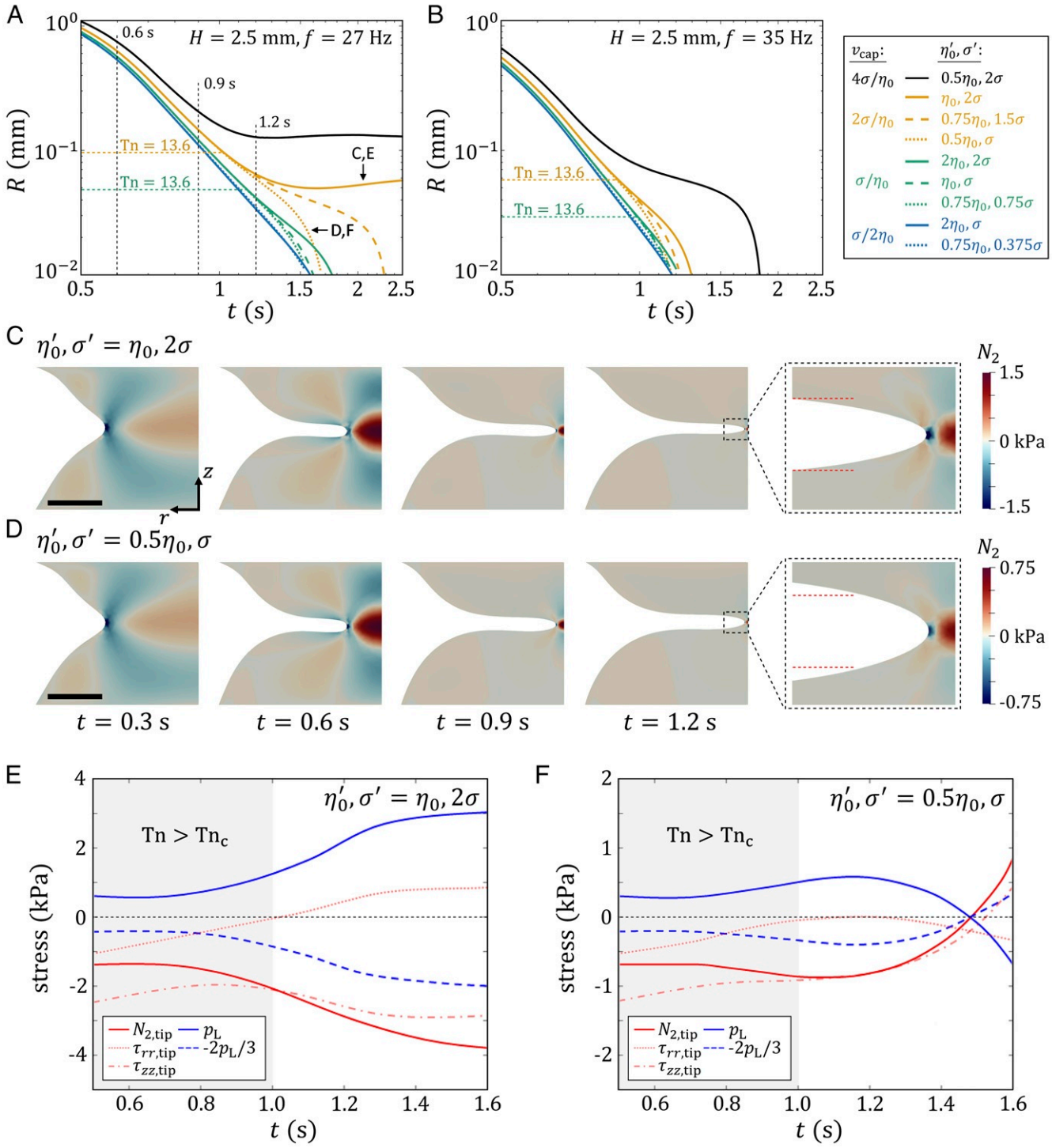

Fig. 7. Simulation of liquid bridge breakup dynamics of fluids with different viscosities η_0' and surface tensions σ'. (*A* and *B*) Radius evolution $R(t)$ of liquid bridges of $H = 2.5$ mm under rotational rates of $f = 27$ and 35 Hz. Each color represents one of the four capillary velocities $v_{\mathrm{cap}} = \sigma'/\eta_0'$. (*C* and *D*) Liquid bridges with $(\eta_0', \sigma') = (\eta_0, 2\sigma)$ and $(0.5\eta_0, \sigma)$ of $H = 2.5$ mm breaking up with a rotational rate $f = 27$ Hz. (Scale bar: 1mm.) (*E* and *F*) Second-normal stress difference $N_{2,\mathrm{tip}}$, normal stresses $\tau_{zz,\mathrm{tip}}$, $\tau_{rr,\mathrm{tip}}$, and Laplace pressure p_{L} at the indent tip of the liquid bridges in *C* and *D*.

but different viscosities η_0' and average relaxation times $\bar{\lambda}'$. Fig. 6*A* shows the best-fit power-law index β of the radius evolution $R(t) \propto t^{-\beta}$ as a function of the plate rotational frequency f. The power-law index β increases as f increases. However, the data points are dispersed. Fig. 6*B* shows β as a function of the Tanner number $\mathrm{Tn}_{R=R_\mathrm{p}} = \bar{\lambda}'\eta_0' R_\mathrm{p}\Omega^2/\sigma$, defined using the plate radius $R_\mathrm{p} = 2.85$ mm. The power-law index β increases with Tn. Also, the data points are seen to collapse onto a single line $\beta = 0.78\ln(\mathrm{Tn}) - 2$ (dotted line in Fig. 6*B*), suggesting that for the same Tanner number $\mathrm{Tn}_{R=R_p}$, the power-law index β of the indent propagation is the same for all four silicone oils used in the liquid bridge experiments.

Next, in the simulation we keep the relaxation times λ_i and mobility parameter α fixed. We vary the surface tension from σ to σ'. We also vary the polymer viscosities from η_i to η_i' (shifting the curves in Fig. 2 *B–D* vertically), which scales the viscosity from η to η' and normal stress coefficients from Ψ_1, Ψ_2 to Ψ_1', Ψ_2' by the same factor. Fig. 7*A* shows radius evolution $R(t)$ of the liquid bridges for $f = 27$ Hz. Fig. 7*A* contains nine sets of $\{\eta_0', \sigma'\}$, which can be divided into four groups with capillary velocities $v_\mathrm{cap} \equiv \sigma'/\eta_0' = 4\sigma/\eta_0$, $2\sigma/\eta_0$, σ/η_0, and $\sigma/2\eta_0$. With $v_\mathrm{cap} = \sigma/\eta_0$ fixed (Fig. 7*A*, green curves), the radius evolution $R(t)$ is independent of the numerical values of $\{\eta_0', \sigma'\}$ until R becomes small enough. The green curves overlap and follow power-law decay until the Tanner number $\mathrm{Tn} = \bar{\lambda}\eta_0' R\Omega^2/\sigma'$ decreases below a critical value $\mathrm{Tn_c} \approx 13.6$. For $\mathrm{Tn} < \mathrm{Tn_c}$, capillary stress dominates normal stress; curves with higher numerical values of σ' decay slower. Increasing v_cap to $2\sigma/\eta_0$ (Fig. 7*A*, orange curves) magnifies the capillary effect, which decreases the slope of $R(t)$ and slows down indent propagation. For $\mathrm{Tn} < \mathrm{Tn_c}$, the curves of $v_\mathrm{cap} = 2\sigma/\eta_0$ diverge more than the previous case of $v_\mathrm{cap} = \sigma/\eta_0$. An obvious example is $\{\eta_0', \sigma'\} = \{\eta_0, 2\sigma\}$ (Fig. 7*A*, orange solid curve). Here, the curve plateaus when $\mathrm{Tn} < \mathrm{Tn_c}$, signifying that the capillary effect is strong enough to completely arrest indent propagation. For the extreme case of $v_\mathrm{cap} = 4\sigma/\eta_0$ (Fig. 7*A*, black solid curve), the capillary effect becomes even stronger. Hence, indent propagation becomes even slower and halts even sooner. For another extreme where $v_\mathrm{cap} = \sigma/2\eta_0$ (Fig. 7*A*, blue curves), the capillary effect is weaker and thus divergence of curves is much less obvious than in all other cases. Fig. 7*B* shows $R(t)$ of the liquid bridges subjected to a higher rotational rate $f = 35$ Hz for the same nine sets of $\{\eta_0', \sigma'\}$. Similar to Fig. 7*A*, the green and orange curves also diverge for $\mathrm{Tn} < \mathrm{Tn_c} \approx 13.6$. However, for larger f, magnitudes of the normal stresses are increased and hence the opposing effect of surface tension becomes relatively smaller. As a result, the curves diverge less and no plateaus of the radius can be observed compared to the previous cases for $f = 27$ Hz. To show that the indent propagation is independent of the elasto-capillary number $\mathrm{Ec} = \bar{\lambda}\sigma/\eta_0 R$, we vary the relaxation times from λ_i to λ_i'. The variation is done such that the term $\bar{\lambda}'\eta_0'\Omega^2/\sigma'$ in Tn is a constant and only $\bar{\lambda}'\sigma'/\eta_0'$ in Ec varies. For $\mathrm{Tn} > \mathrm{Tn_c} \approx 13.6$, increasing $\bar{\lambda}'\sigma'/\eta_0'$ shifts $R(t)$ horizontally leftward and leaves the slope of $R(t)$ constant (*SI Appendix*, Fig. S3). Hence, the indent propagation process is indeed independent of Ec and is solely governed by Tn.

Such sole dependence of the indent propagation on the Tanner number Tn signifies certain similarities in the indentation shapes and stress fields for liquid bridges having the same capillary velocity v_cap. Fig. 7 *C* and *D* shows the time evolution of the indentation shapes and second-normal stress differences N_2 of two liquid bridges with $\{\eta_0', \sigma'\} = \{\eta_0, 2\sigma\}$ and $\{0.5\eta_0, \sigma\}$. Both of the liquid bridges have $v_\mathrm{cap} = 2\sigma/\eta_0$ and are subjected to a plate rotation of $f = 27$ Hz. The two cases correspond to two of the orange curves in Fig. 7*A*; the former one labeled *C* reaches a plateau radius and the latter one labeled *D* approaches zero. For $t = 0.3$, 0.6, and 0.9 s at which $\mathrm{Tn} > \mathrm{Tn_c}$, both the indent shapes and N_2 distributions appear to be the same for the two cases, except that the maximum and minimum N_2 values in Fig. 7*C* are scaled by a factor of 2 from those in Fig. 7*D*. As the two cases have the same plate sizes and rotational speeds, we can further infer that the indent propagation is driven by a local balance between the surface tension and normal stresses around the indent tip. Zoomed-in versions of the indentation shapes over time can be found in *SI Appendix*, Fig. S4. For $t = 1.2$ s at which $\mathrm{Tn} > \mathrm{Tn_c}$, indent shapes and N_2 distributions of the two cases start to differ. For instance, as shown in Fig. 7 *C* and *D*, *Insets*, the indent size for the case of $\{\eta_0', \sigma'\} = \{\eta_0, 2\sigma\}$ becomes smaller than that of $\{\eta_0', \sigma'\} = \{0.5\eta_0, \sigma\}$; as a consequence, shear is more localized and magnitude of the negative N_2 is larger around the indent tip.

The Tanner–Keentok criterion informs us that N_2 and p_L are critical to interpret what we have observed in Fig. 7 *A–D*. Fig. 7 *E* and *F* shows for the cases of $\{\eta_0', \sigma'\} = \{\eta_0, 2\sigma\}$ and $\{0.5\eta_0, \sigma\}$ the second-normal stress difference $N_{2,\mathrm{tip}}$ (red solid curves) and the Laplace pressure p_L (blue solid curves) at the indent tip as functions of time t. The normal stresses $\tau_{zz,\mathrm{tip}}$ and $\tau_{rr,\mathrm{tip}}$ (red dotted curves) and the Tanner–Keentok criterion (blue dotted curves) are also shown here to be compared with $N_{2,\mathrm{tip}}$. For 0.5 s $< t <$ 1 s when $\mathrm{Tn} > \mathrm{Tn_c}$ (Fig. 7 *E* and *F*, gray area), $N_{2,\mathrm{tip}}$ and p_L show the same trend in both cases and differ only by a factor of 2 in terms of their magnitudes. At $t \approx 0.5$ s, the liquid bridge radius $R \approx 1$ mm and height $H = 2.5$ mm are both at least an order of magnitude larger than the radius of curvature $a \approx 0.07$ mm of the indent tip, which matches the assumptions of the Tanner–Keentok criterion (note that those assumptions become less and less adequate as R decreases). The Tanner–Keentok criterion $|N_2| > 2p_\mathrm{L}/3 \approx 2\sigma/3a$ is satisfied, providing further evidence that for $\mathrm{Tn} > \mathrm{Tn_c}$ the indent formation is driven by edge fracture. For 0.5 s $< t <$ 0.8 s, the Laplace pressure p_L appears constant since the radius of curvature a of the indent tip does not change much during this timespan (Fig. 7 *C* and *D* and *SI Appendix*, Fig. S4). As the liquid bridge radius R decreases, the effective shear rate $R\Omega/2a$ at the indent tip also decreases, making magnitudes of the normal stress components $\tau_{zz,\mathrm{tip}}$ and $\tau_{rr,\mathrm{tip}}$ decrease with time. However, the difference $\tau_{zz,\mathrm{tip}} - \tau_{rr,\mathrm{tip}}$ remains approximately a constant for 0.5 s $< t <$ 0.8 s. Therefore, the second-normal stress difference $N_{2,\mathrm{tip}}$ remains constant during this timespan just like the Laplace pressure p_L. For $t > 1.1$ s when $\mathrm{Tn} < \mathrm{Tn_c}$ (Fig. 7 *E* and *F*, white area), the trends of $N_{2,\mathrm{tip}}$ and p_L in Fig. 7 *E* and *F* start to differ. In this region, as the liquid bridge radius R becomes comparable with the indent radius of curvature a, the Tanner–Keentok criterion is no longer applicable. We need to consider capillary effects to explain the difference between Fig. 7*E* and 7*F*. For the $\{\eta_0', \sigma'\} = \{\eta_0, 2\sigma\}$ case (Fig. 7*E*) $N_{2,\mathrm{tip}}$ and p_L diverge from each other and reach their plateau at $t \approx 1.5$ s. Here, the Laplace pressure $p_\mathrm{L} = \sigma(1/a - 1/R)$ never changes sign, implying that the liquid bridge radius R never reaches a. Instead, as the lower portion of the liquid bridge reconfigures to a hemispherical shape by surface tension, the indent radius of curvature a decreases over time, which causes p_L to increase over time. The decrease of a also makes shear around the indent tip more concentrated, which decreases $N_{2,\mathrm{tip}}$ over time. On the other hand, the $\{\eta_0', \sigma'\} = \{0.5\eta_0, \sigma\}$ case (Fig. 7*F*) has a lower surface tension and thus capillary reconfiguration is slower. Both $N_{2,\mathrm{tip}}$ and p_L change sign at $t \approx 1.5$ s, signifying that the second-normal stress difference becomes stabilizing and the surface tension becomes destabilizing as R becomes smaller than a.

Discussion and Conclusion

Combining high-speed imaging and viscoelastic flow simulation, we show that torsion can break viscoelastic liquid bridges effectively. Using a setup consisting of two concentric circular plates, one rotatable and one vertically translatable, we demonstrate

that a concave surface can localize shear around the liquid bridge's neck even for a Newtonian fluid. For a viscoelastic fluid, the localized shear can induce normal stresses that in turn make the surface more concave. Such positive feedback creates an indent of size $2a$ that propagates toward the center and leads to quick breakup of the liquid bridge. The indent formation process and its associated flow patterns resemble edge fracture, a flow instability often observed when a viscoelastic fluid is sheared in a thin gap (14–20). For capillary stable bridges, edge fracture causes the radius R to undergo power-law decay $R \propto t^{-\beta}$ with a power-index β that increases with increasing rotational rate f. Edge fracture takes place until the Tanner number $\mathrm{Tn} = \lambda\eta_0 R\Omega^2/\sigma$, which characterizes the relative importance of normal and capillary stresses, reaches a small enough critical value $\mathrm{Tn_c} \approx 13.6$. For $\mathrm{Tn} < \mathrm{Tn_c}$, surface tension governs how the liquid bridge radius R evolves. For small $R \approx a$ and high surface tension such as $\sigma = 41.2$ mN/m, the lower portion of the liquid bridge reconfigures to a hemispherical shape, which decreases the indent size a and increases the Laplace pressure p_L over time. As a result, p_L never changes sign and the liquid bridge radius R never reaches a. For lower surface tension such as $\sigma = 20.6$ mN/m, capillary reconfiguration is slower. The indent propagation is quick enough such that R can reach a, which changes the sign of p_L and causes surface tension to destabilize the liquid bridge.

Edge fracture renders rheological measurement results of viscoelastic fluids at high shear rate inaccurate and hard to interpret (14–20). Because of this, experimentalists have invented different gadgets, such as specially designed guard rings (41) and the cone-partitioned-plate geometry (42–44), to bypass the negative effects of edge fracture. In contrast, our study takes advantage of edge fracture for potential practical applications. By applying torsion, edge fracture occurs, creating an indent that propagates toward the center of the viscoelastic liquid bridge. In this way, even short, capillary stable liquid bridges can be broken in $\mathcal{O}(1$ s). For industries that require quick and clean dispensing of viscoelastic fluids, this may prevent the substrate from being contaminated by the satellite droplets (4) and long capillary tails (12) formed by stretching the liquid bridge. On the other hand, theorists have proposed different theories (14–16, 18, 19) to explain how edge fracture occurs. Essentially, those theoretical studies assumed a planar Couette flow, which corresponds to liquid bridges with $R \gg H$. Also, they focused only on the onset of edge fracture and did not consider its propagation process. Therefore, the parameter space of edge fracture explored so far has been highly limited. Compared to the planar Couette flow, liquid bridges considered in our study have radius $R \approx H$. Although this made the flow field no longer a simple shear flow, this extended the parameter space of edge fracture research and allowed much clearer experimental visualization of the fluid interface that contains the most critical information (surface curvature, indent size, radius evolution) of edge fracture. Indeed, this is what enabled us to study the propagation of edge fracture and to directly compare our experimental and simulation results, which would otherwise be very difficult for a planar Couette flow.

As a remark, we note that viscoelastic fluids are also known to undergo fracture under extension (45–48). For instance, Huang et al. (46) reported for two model entangled polymer solutions that liquid bridges under uniaxial extension demonstrated multiple-crack propagation behavior. The cracks propagate at constant speed and their profiles can be qualitatively described by the viscoelastic trumpet model (49) with the crack tip showing brittle fracture behavior. Wagner et al. (48) subsequently developed the entropic fracture model to explain such extensional fracture behavior: thermal fluctuations lead to temporary concentration of strain energy, which causes the polymer chain to rupture and initiates crack propagation in the liquid bridge. In contrast to the extensional fracture, the torsional edge fracture that we have described in this work shows power-law indent propagation behavior; thus, the viscoelastic trumpet model is not applicable. Also, there is no rupture of polymer chains assumed in our viscoelastic simulation, so the entropic fracture model does not apply. Hence, the extensional fracture of viscoelastic fluids is not related to the torsional edge fracture described in the current study; readers should not be confused between the two phenomena.

Future work is needed to address several remaining points from our study. First, why does the indent caused by edge fracture have a rather constant size throughout its propagation process? Second, the indent propagation caused by edge fracture shows power-law behavior and depends solely on the Tanner number Tn, which hints at the existence of a similarity solution. An analytical form of such a solution may help develop efficient methods to measure material properties such as the normal stress coefficients. Does such a solution exist? Third, so far we have considered only viscoelastic liquid bridges with a relaxation time $\lambda \in \mathcal{O}(1$ ms), which gives an elasto-capillary number $\mathrm{Ec} \ll 1$. What other phenomena can be observed for fluids with a much higher λ? In addition, the simulation results presented in Fig. 5 are not yet verified by experiments. Identifying suitable fluids with the desired mobility parameter will be a topic of future research. Finally, edge fracture is also known to occur in suspensions and pastes (15). How will a finite yield stress in such fluids affect the indent propagation process? Addressing the first four points will lead to a better physical understanding of edge fracture. The last point is important for practical applications, such as the dispensing of functional fluids that are viscoelastic with yield stress nature (50–52).

Materials and Methods

Experimental Protocol. The experimental model system consists of an upper rotatable plate and a lower vertically translatable plate, both of which are circular with radius $R_\mathrm{p} = 2.85$ mm. To apply unidirectional rotation with minimal mechanical vibration, the upper plate was directly connected to the shaft of a DC metal brush motor (Mabuchi Motor RE-280A). As the experimental results agreed well with both the Newtonian and the viscoelastic flow simulations, in which no vibration was imposed, slight vibration of the motor shaft in our experiments was assumed to have a negligible effect on the liquid bridge thinning process. The lowest accessible rotational rate of the upper plate is 13.3 Hz. The time t_f that the motor needs to achieve its full speed was estimated to be 1 s. Such estimation was done by varying t_f in the simulation until the simulation and experimental results match quantitatively. To apply vertical movement, the lower plate was connected to a computer-controlled dip coater (Nima Technology Ltd.). A single constant vertical speed of 0.67 mm/s was applied to the bottom plate. Fluid of 40 μL was injected between the two plates using a positive displacement pipette (MICROMAN; Gilson). The liquid bridge was illuminated using a high-intensity light-emitting diode (LED) light source (Fiber-Lite MI-LED; Dolan-Jenner Industries) connected to a 52-mm telecentric backlight illuminator (TECHSPEC; Edmund Optics). High-speed videos of the liquid bridge thinning were captured using a high-speed camera (FASTCAM Mini AX100; Photron USA Inc.) with a frame rate of 50 fps, a shutter speed of 10,000 Hz, and a 12× zoom, 12-mm fine focus objective lens (Navitar Inc.). To eliminate experimental error due to volume variation of the liquid bridge, the same droplet of fluid was used for each set of experiments, which consisted of sweeping the rotational rate of the upper plate through a list of discrete values twice. Each set of experiments was conducted in the same day. Evaporation of the liquid bridge is negligible due to the high-molecular-weight nature of the fluids used.

Material Characterization. A strain-controlled rheometer (ARES-G2; TA Instruments) was used to measure rheology of Infineum S1054 (Infineum Japan Ltd.) and the silicone oil (Dow Corning 200; Sigma-Aldrich). For Infineum S1054, the steady-shear test was performed with a 40-mm diameter stainless steel 1° cone-and-plate geometry to obtain the flow curve in a shear-rate range of 1 to 300 s^{-1} at 25 °C. For the silicone oil, the SAOS test

was performed with a 10-mm diameter stainless-steel parallel plate geometry to obtain the storage modulus G' and the loss modulus G'' in a frequency range of 1 to 300 rad/s in a temperature range of -65 to 25 °C. The strain amplitude was 5%, which ensures that the silicone oil being measured was in the linear viscoelastic regime, where G' and G'' are independent of the strain amplitude (53). The rheometer was connected to a liquid nitrogen tank and the temperature was decreased using the liquid nitrogen controller (TA Instruments). The data obtained at different temperatures were used to construct a master curve at 25 °C (symbols in Fig. 2*B*) using the time–temperature superposition principle (54). The multimode Maxwell model (lines in Fig. 2*B*), which corresponds to the low-strain limit of the multimode Giesekus model (24), was then used to fit the master curve to get the polymer viscosities and relaxation times of the silicone oil, which were used in the viscoelastic flow simulation. On the other hand, to verify that the Giesekus model predicts the correct rheological behaviors of the silicone oil, the steady-shear test was performed to obtain the first- and second-normal stress differences (N_1, N_2) in a shear-rate range of 10 to 100 s^{-1} at 25 °C. A 40-mm diameter stainless-steel 1° cone-and-plate geometry was used to obtain N_1, while a 40-mm stainless-steel parallel plate geometry was used to obtain $N_1 - N_2$ (55). Here, a sudden drop in the shear stress was measured at a shear rate of $\dot{\gamma} \approx 60$ s^{-1} for the cone-and-plate geometry and $\dot{\gamma} \approx 30$ s^{-1} for the parallel plate geometry. Hence, data above those shear rates were discarded. Nonetheless, both the N_1 and $N_1 - N_2$ data agreed well with the Giesekus model prediction, both of which are shown in Fig. 2 *C* and *D*. An optical tensiometer (Theta Attension; Biolin Scientific) was used to measure surface tension of both Inifineum S1054 and the silicone oil by the pendant drop method (56) at 25 °C. Rheology and surface tension of the three additional silicone oils described in Fig. 6 were measured with the same protocol aforementioned. The 48.1-Pa·s sample is a mixture of the 32.3-Pa·s sample (silicone oil viscosity 30,000 cSt; Sigma-Aldrich) and the 58.6-Pa·s sample used in most of our studies. The 78-Pa·s sample is a mixture of the 58.6-Pa·s sample and a 109-Pa·s sample (silicone oil viscosity 100,000 cSt; Sigma-Aldrich).

Image Analysis. The high-speed videos were analyzed using in-house developed image analysis software, using Matlab (MathWorks). The region of interest (ROI) was cropped using the inbuilt function getrect. The cropped image was converted into a double-precision image from RGB using the im2double function, which scales the output from integer data types to the range [0, 1]. Next, the image was converted to a binary image with a threshold value of 0.75 using im2bw. The image defects were adjusted using the imfill function with threshold value of 0.4. Next, a raster scan was performed row by row on the ROI to determine the edge profile of the bridge by computing the largest-intensity gradient at every pixel between the bridge and background. The liquid bridge's neck radius R was computed by determining the thinnest point of the bridge profile. The process was repeated for the entire radius evolution. Volume of the liquid bridge was determined from the bridge profile by the solid of revolution method and was confirmed to be 40 ± 0.2 μL.

Simulations. To simulate the flow, the momentum and mass balance equations for incompressible fluids (57) were solved:

$$\rho\left(\partial_t \boldsymbol{v} + \boldsymbol{v}\cdot\nabla\boldsymbol{v}\right) = \nabla\cdot\left(-p\boldsymbol{I} + 2\eta_s\boldsymbol{D} + \boldsymbol{\tau}\right) + \rho\boldsymbol{g}, \quad [3]$$

$$\nabla\cdot\boldsymbol{v} = 0. \quad [4]$$

Here, p, $\boldsymbol{I}$, and η_s are the pressure, unity tensor, and Newtonian viscosity, respectively. Gravity was introduced as a body force $\boldsymbol{g}$ along the negative z direction. To solve the governing equations for the Newtonian Infineum S1054 fluid, the Newtonian viscosity was used: $\eta_s = \eta$ and $\boldsymbol{\tau} = \boldsymbol{0}$. In the case of the viscoelastic silicone oil, the Newtonian viscosity was used as a solvent viscosity and the viscoelastic stress tensor was solved using the multimode Giesekus model given in Eqs. **1** and **2**. Here, the equations were discretized using a method described in ref. 57 and solved using the stabilized finite-element method, whose mesh method, mesh movement and projection, time stepping, and stabilization can be found in ref. 58. Boundary conditions of the simulation were no slip on the plate boundaries and surface tension on the free surface of the liquid bridge. Because the experimental system is rotationally symmetric, axisymmetric flow with swirl was assumed in the simulation. Hence, a two-dimensional geometry was used. The unknown fields $\boldsymbol{\tau}$, $\boldsymbol{v}$, and p depend on r, z, and θ in the cylindrical coordinate system and the gradients in the azimuthal direction are zero. Before the simulation starts, the material was assumed to be stagnant and stress-free. In the experiments with the Newtonian fluid (Infineum S1054), the sample was first deposited between two concentric plates with an initial separation $H_0 = 2.5$ mm. The sample was then prestretched with a velocity 0.67 mm/s to a final separation H. After that, the rotational rate of the upper plate was increased linearly from 0 to f within a timespan t_f. The same process was reproduced in the Newtonian simulation. In the case of the viscoelastic silicone oil, no prestretch was applied in the experiments. The starting geometry used in all viscoelastic simulations was directly extracted from the experimental images.

Data Availability. All study data are included in this article and/or *SI Appendix*.

ACKNOWLEDGMENTS. S.T.C., A.M., S.J.H., and A.Q.S. acknowledge the support of Okinawa Institute of Science and Technology Graduate University with subsidy funding from the Cabinet Office, Government of Japan. S.T.C., A.M., S.J.H., and A.Q.S. also acknowledge financial support from the Japanese Society for the Promotion of Science (JSPS) (Grants 21J10517, 19K15641, 18K03958, 21K03884, and 18H01135) and the Joint Research Projects supported by the JSPS and the Swiss National Science Foundation. F.P.A.v.B. and P.D.A. thank Dr. M. A. Hulsen for providing access to the Toolkit for Finite Element Method software libraries. S.T.C. and H.A.F. thank Prof. H. C. Shum for fruitful discussions that helped conceive the research idea. We thank Prof. G. H. McKinley and Prof. R. I. Tanner for helpful comments.

1. G. H. McKinley, Visco-elasto-capillary thinning and break-up of complex fluids. *Rheol. Rev.* **3**, 1–48 (2005).
2. T. E. Karis, An overview of rheology in the computer industry. *J. Appl. Polym. Sci.* **59**, 1405–1416 (1996).
3. X. B. Chen, Modeling and control of fluid dispensing processes: A state-of-the-art review. *Int. J. Adv. Manuf. Technol.* **43**, 276–286 (2009).
4. C. Clasen, P. M. Phillips, L. Palangetic, J. Vermant, Dispensing of rheologically complex fluids: The map of misery. *AIChE J.* **58**, 3242–3255 (2012).
5. G. Tabilo-Munizaga, G. V. Barbosa-Cánovas, Rheology for the food industry. *J. Food Eng.* **67**, 147–156 (2005).
6. M. E. Mackay, The importance of rheological behavior in the additive manufacturing technique material extrusion. *J. Rheol.* **62**, 1549–1561 (2018).
7. L. A. Slobozhanin, J. M. Perales, Stability of liquid bridges between equal disks in an axial gravity field. *Phys. Fluids A* **5**, 1305–1314 (1993).
8. G. H. McKinley, A. Tripathi, How to extract the Newtonian viscosity from capillary breakup measurements in a filament rheometer. *J. Rheol.* **44**, 653–670 (2000).
9. J. Li, G. Deng, "Technology development and basic theory study of fluid dispensing-a review" in *Proceedings of the Sixth IEEE CPMT Conference on High Density Microsystem Design and Packaging and Component Failure Analysis (HDP'04)*, J. Liu, T. Yu, Eds. (IEEE, Shanghai, China, 2004), pp. 198–205.
10. D. T. Papageorgiou, On the breakup of viscous liquid threads. *Phys. Fluids* **7**, 1529–1544 (1995).
11. S. L. Anna, G. H. McKinley, Elasto-capillary thinning and breakup of model elastic liquids. *J. Rheol.* **45**, 115–138 (2001).
12. B. L. Toh, H. K. Yeoh, W. H. Teoh, L. C. Chin, Surface mount adhesive: In search of a perfect dot. *Int. J. Adv. Manuf. Technol.* **90**, 2083–2094 (2017).
13. S. Kumar, Liquid transfer in printing processes: Liquid bridges with moving contact lines. *Annu. Rev. Fluid Mech.* **47**, 67–94 (2015).
14. R. I. Tanner, M. Keentok, Shear fracture in cone-plate rheometry. *J. Rheol.* **27**, 47–57 (1983).
15. M. Keentok, S. C. Xue, Edge fracture in cone-plate and parallel plate flows. *Rheol. Acta* **38**, 321–348 (1999).
16. E. J. Hemingway, S. M. Fielding, Edge fracture instability in sheared complex fluids: Onset criterion and possible mitigation strategy. *J. Rheol.* **63**, 735–750 (2019).
17. C. S. Lee, B. C. Tripp, J. J. Magda, Does N_1 or N_2 control the onset of edge fracture? *Rheol. Acta* **31**, 306–308 (1992).
18. R. R. Huilgol, M. Panizza, L. E. Payne, On the rectilinear flow of a second-order fluid and the role of the second normal stress difference in edge fracture in rheometry. *J. Non-Newt. Fluid Mech.* **50**, 331–348 (1993).
19. E. J. Hemingway, S. M. Fielding, Interplay of edge fracture and shear banding in complex fluids. *J. Rheol.* **64**, 1147–1159 (2020).
20. O. Maklad, R. J. Poole, A review of the second normal-stress difference; its importance in various flows, measurement techniques, results for various complex fluids and theoretical predictions. *J. Non-Newt. Fluid Mech.* **292**, 104522 (2021).
21. J. Eggers, E. Villermaux, Physics of liquid jets. *Rep. Prog. Phys.* **71**, 036601 (2008).
22. K. Verhulst, R. Cardinaels, P. Moldenaers, Y. Renardy, S. Afkhami, Influence of viscoelasticity on drop deformation and orientation in shear flow. Part 1: Stationary states. *J. Non-Newt. Fluid Mech.* **156**, 29–43 (2009).
23. K. Verhulst, R. Cardinaels, P. Moldenaers, S. Afkhami, Y. Renardy, Influence of viscoelasticity on drop deformation and orientation in shear flow. Part 2: Dynamics. *J. Non-Newt. Fluid Mech.* **156**, 44–57 (2009).
24. F. Snijkers *et al.*, Effect of viscoelasticity on the rotation of a sphere in shear flow. *J. Non-Newt. Fluid Mech.* **166**, 363–372 (2011).

25. R. Cardinaels, S. Afkhami, Y. Renardy, P. Moldenaers, An experimental and numerical investigation of the dynamics of microconfined droplets in systems with one viscoelastic phase. *J. Non-Newt. Fluid Mech.* **166**, 52–62 (2011).
26. H. Giesekus, A simple constitutive equation for polymer fluids based on the concept of deformation-dependent tensorial mobility. *J. Non-Newt. Fluid Mech.* **11**, 69–109 (1982).
27. H. Giesekus, Stressing behaviour in simple shear flow as predicted by a new constitutive model for polymer fluids. *J. Non-Newt. Fluid Mech.* **12**, 367–374 (1983).
28. R. G. Larson, *Constitutive Equations for Polymer Melts and Solutions* (Butterworths, 1988).
29. T. Holz, P. Fischer, H. Rehage, Shear relaxation in the nonlinear-viscoelastic regime of a Giesekus fluid. *J. Non-Newt. Fluid Mech.* **88**, 133–148 (1999).
30. A. K. Gurnon, N. J. Wagner, Large amplitude oscillatory shear (LAOS) measurements to obtain constitutive equation model parameters: Giesekus model of banding and nonbanding wormlike micelles. *J. Rheol.* **56**, 333–351 (2012).
31. S. Chen, J. P. Rothstein, Flow of a wormlike micelle solution past a falling sphere. *J. Non-Newt. Fluid Mech.* **116**, 205–234 (2004).
32. A. Bhardwaj, E. Miller, J. P. Rothstein, Filament stretching and capillary breakup extensional rheometry measurements of viscoelastic wormlike micelle solutions. *J. Rheol.* **51**, 693–719 (2007).
33. A. S. Khair, Large amplitude oscillatory shear of the Giesekus model. *J. Rheol.* **60**, 257–266 (2016).
34. M. F. Tomé, M. T. Araujo, J. Evans, S. McKee, Numerical solution of the Giesekus model for incompressible free surface flows without solvent viscosity. *J. Non-Newt. Fluid Mech.* **263**, 104–119 (2019).
35. N. O. Jaensson, M. A. Hulsen, P. D. Anderson, Direct numerical simulation of particle alignment in viscoelastic fluids. *J. Non-Newt. Fluid Mech.* **235**, 125–142 (2016).
36. M. A. Carrozza, M. A. Hulsen, M. Hütter, P. D. Anderson, Viscoelastic fluid flow simulation using the contravariant deformation formulation. *J. Non-Newt. Fluid Mech.* **270**, 23–35 (2019).
37. J. D. Evans, M. L. Evans, The extrudate swell singularity of Phan-Thien-Tanner and Giesekus fluids. *Phys. Fluids* **31**, 113102 (2019).
38. R. B. Bird, J. M. Wiest, Anisotropic effects in dumbbell kinetic theory. *J. Rheol.* **29**, 519–532 (1985).
39. N. Phan-Thien, R. I. Tanner, A new constitutive equation derived from network theory. *J. Non-Newt. Fluid Mech.* **2**, 353–365 (1977).
40. M. W. Johnson Jr., D. Segalman, A model for viscoelastic fluid behavior which allows non-affine deformation. *J. Non-Newt. Fluid Mech.* **2**, 255–270 (1977).
41. S. E. Mall-Gleissle, W. Gleissle, G. H. McKinley, H. Buggisch, The normal stress behaviour of suspensions with viscoelastic matrix fluids. *Rheol. Acta* **41**, 61–76 (2002).
42. F. Snijkers, D. Vlassopoulos, Cone-partitioned-plate geometry for the ARES rheometer with temperature control. *J. Rheol.* **55**, 1167–1186 (2011).
43. T. Schweizer, W. Schmidheiny, A cone-partitioned plate rheometer cell with three partitions (CPP3) to determine shear stress and both normal stress differences for small quantities of polymeric fluids. *J. Rheol.* **57**, 841–856 (2013).
44. S. Costanzo, G. Ianniruberto, G. Marrucci, D. Vlassopoulos, Measuring and assessing first and second normal stress differences of polymeric fluids with a modular cone-partitioned plate geometry. *Rheol. Acta* **57**, 363–376 (2018).
45. C. Ligoure, S. Mora, Fractures in complex fluids: The case of transient networks. *Rheol. Acta* **52**, 91–114 (2013).
46. Q. Huang, N. J. Alvarez, A. Shabbir, O. Hassager, Multiple cracks propagate simultaneously in polymer liquids in tension. *Phys. Rev. Lett.* **117**, 087801 (2016).
47. Q. Huang, O. Hassager, Polymer liquids fracture like solids. *Soft Matter* **13**, 3470–3474 (2017).
48. M. H. Wagner, E. Narimissa, Q. Huang, On the origin of brittle fracture of entangled polymer solutions and melts. *J. Rheol.* **62**, 221–233 (2018).
49. P. G. De Gennes, Soft adhesives. *Langmuir* **12**, 4497–4500 (1996).
50. C. Billotte, P. J. Carreau, M. C. Heuzey, Rheological characterization of a solder paste for surface mount applications. *Rheol. Acta* **45**, 374–386 (2006).
51. R. Lapasin, V. Sirtori, D. Casati, Rheological characterization of solder pastes. *J. Electron. Mater.* **23**, 525–532 (1994).
52. J. Zhou, E. Sancaktar, Yield behavior of moderately filled epoxy/Ni suspensions. *J. Adhes. Sci. Technol.* **24**, 1929–1948 (2010).
53. F. A. Morrison, *Understanding Rheology* (Oxford University Press, 2001).
54. J. D. Ferry, *Viscoelastic Properties of Polymers* (John Wiley & Sons, 1980).
55. M. Keentok, R. I. Tanner, Cone-plate and parallel plate rheometry of some polymer solutions. *J. Rheol.* **26**, 301–311 (1982).
56. J. D. Berry, M. J. Neeson, R. R. Dagastine, D. Y. C. Chan, R. F. Tabor, Measurement of surface and interfacial tension using pendant drop tensiometry. *J. Colloid Interface Sci.* **454**, 226–237 (2015).
57. C. Mitrias, N. O. Jaensson, M. A. Hulsen, P. D. Anderson, Head-on collision of Newtonian drops in a viscoelastic medium. *Microfluid. Nanofluidics* **23**, 87 (2019).
58. F. P. A. Van Berlo, R. Cardinaels, G. W. M. Peters, P. D. Anderson, A numerical study of extensional flow-induced crystallization in filament stretching rheometry. *Polym. Cryst.* **4**, e10154 (2020).